5th International Conference on Experimental Fluid Mechanics ICEFM 2018 Munich
Munich, Germany, July 2-4, 2018

Energies of laser-induced cavitation bubbles and emitted shock waves using Differential Interferometry

Stephan Kordel[1*] **and Jeanette Hussong**[1]

[1] Research Group Laser Measurement Techniques in Multiphase Flows,Chair of Hydraulic Fluid Machinery, Ruhr-Universität Bochum, Germany

[*] stephan.kordel@ruhr-uni-bochum.de

Abstract

In the present study a combination of Shadowgraphy and Differential Interferometry is used to investigate the spatial distribution of pressure waves emanating from laser induced single cavitation bubbles. The accuracy of the evaluation process is determined through synthetic data analysis. Energy budgets of caviation bubbles with initial laser energy of $E_l = 25.2 \pm 0.9\,\mu J$ are determined.

1 Introduction

Laser induced single bubble cavitation originates from a non-linear absorption process when the introduced laser energy leads to an optical breakthrough and the generation of a vapor bubble which collapses during recondensation (Shen, 1984). Both, bubble generation and the implosion of the bubble induce a pressure wave that propagates outwards radially from the bubble center. For asymmetric bubble collapses, emitted pressure waves and liquid jets may occur, being known to be the key mechanisms of cavitation induced surface damage. Collapse times and pressure amplitudes strongly depend on the cavitation bubble dynamics (Vogel and Lauterborn, 1988). Most commonly, these pressure amplitudes are either measured locally with hydrophones (Vogel, 1996) or they are extracted from the shock front velocity based on the momentum conservation (Nagayama et al., 2002). Studies to access cavitation-induced 1D pressure profiles by means of Mach-Zehnder Interferometry have been utilized by Kim et al. (2003) and others (Ward and Emmony, 1991; Veysset et al., 2016). However, their motivation was the extraction of 1D pressure profiles from the interference technique.
In the present study we show how 2D pressure fields inside individual pressure waves can be determined by means of Differential Interferometry. This allows us to determine the bubble energy E_b and pressure wave energy E_s directly from measurements, as the pressure wave field p_s, the pressure wave propagation length R_m and the cavitation bubble radius R_{max} are deducted from the interference and shadowgraph images as follows.

$$E_s = \frac{4\pi R_m^2}{\rho_0 c_0^2} \int p_s^2 dr \tag{1}$$

$$E_b = \frac{4}{3}\pi R_{max}^3 (p_0 - p_v) \tag{2}$$

2 Experimental Set-up

Fig. 1 shows a shematic of the experimental set-up. A frequency doubled Nd:YAG (laser 1, EverGreen 70, Quantel) with 6 ns pulse width is focused into a water filled cuvette (test section). The energy of each laser pulse is measured with an energy meter (RM 3700, Laser Probe Inc.) after being split with a 50/50 mirror. The cavitation bubble dynamics is recorded with a shadowgraphy image system. For this, a camera system (HS cam, Phantom Miro 110, Vision Research) is focused to the expected center of the nucleus with a far-field microscope (K2 DistaMax, Infinity). For background illumination a pulsed LED (pulse width

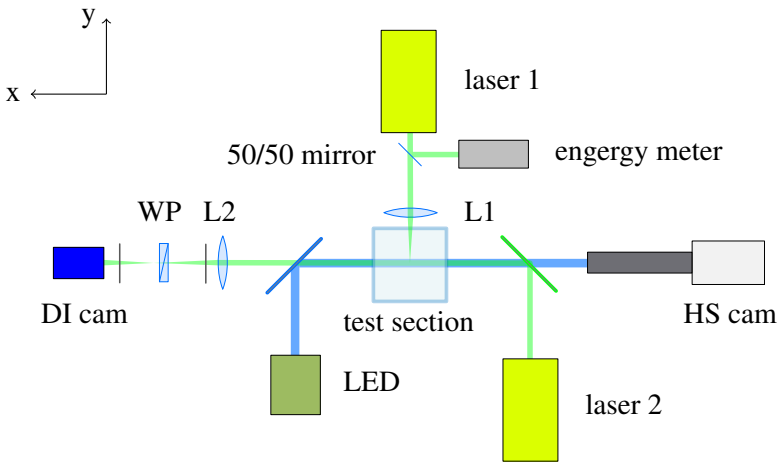

Figure 1: Shematic of optical set-up with combination of Shadowgraphy and Differential Interferometry for bubble dynamics and pressure field measurements

200 ns, $\lambda = 462$ nm) is syncronized to the camera recordings. With a recording rate of 77 000 Hz the bubble evolution until its first collapse can be resolved with approximately 5 frames.
A second double pulsed dual cavity Nd:YAG laser (laser 2, Nano S65, Litron) is used for the Differential Interferometry measurements. The laser beam passes the test section in opposite direction than the LED light path. It is focused by a lens (L2), before passing a Wollaston prism (WP). Interference images are recorded with a double frame CCD camera (DI Cam, Imager ProSX, LaVision), where the first frame captures the initial pressure wave and the second frame the pressure wave after bubble collapse. Time delays were set to 2.5 µs for the first and 55.5 µs for the second frame.
For reference measurements, a needle hydrophone (Mueller Instruments) as well as an oxygen sensor (FireStingO2, pyroscience) and a temperature sensor (PT100) are placed inside the cuvette.

3 Reconstruction of pressure fields

Interferograms are taken with the Differential Interference set-up. Hence, density gradient fields can be determined from phase differences which appear as fringe shifts in the interferogram. These phase differences are caused by different propagation velocities of two adjacent interfering light rays of finite distance d passing through the measuring section of depth b. According to (3) the density gradient perpendicular to the fringes orientation $\partial\rho/\partial\zeta$ is porportional to the relative fringe displacement $\Delta S/S$. Here, the wavelength λ and the Gladstone Dale Konstant K are characteristik quantities of the set-up and the fluid.

$$\frac{\partial\rho}{\partial\zeta} = \frac{\lambda}{Kbd}\frac{\Delta S}{S} \tag{3}$$

Providing that a radially propagating pressure wave behaves in free space as a spherical shell of finite thickness, the actual density gradient in radial direction $\partial\rho/\partial r$ can be calculated from the projected density gradient $\partial\rho/\partial\zeta$. For this purpose, the fringe displacement is evaluated starting from the bubble center in azimuthal direction. To determine fringe centerlines, a local Gaussian fit is applied to minima and maxima of the fringe pattern. From these centerlines the relative fringe displacement field $\Delta S/S$ and hence the density gradient field $\partial\rho/\partial r$ can be determined. Numerical integration provides the density field. Due to the measuring principle, the determined density field represents the projection of the density along the laser light direction. Therefore, inverse Abel Transformation is utilized for reconstruction of spherical pressure waves.

The algorithm was evaluated with synthetically generated pressure wave distributions. Fig. 2(a) shows a synthetic interference pattern and a measured interference pattern. The relative fringe displacement $\Delta S/S$ scales with the measurement sensitivity but also depends on the orientation angle φ. Fig. 2(b) depicts

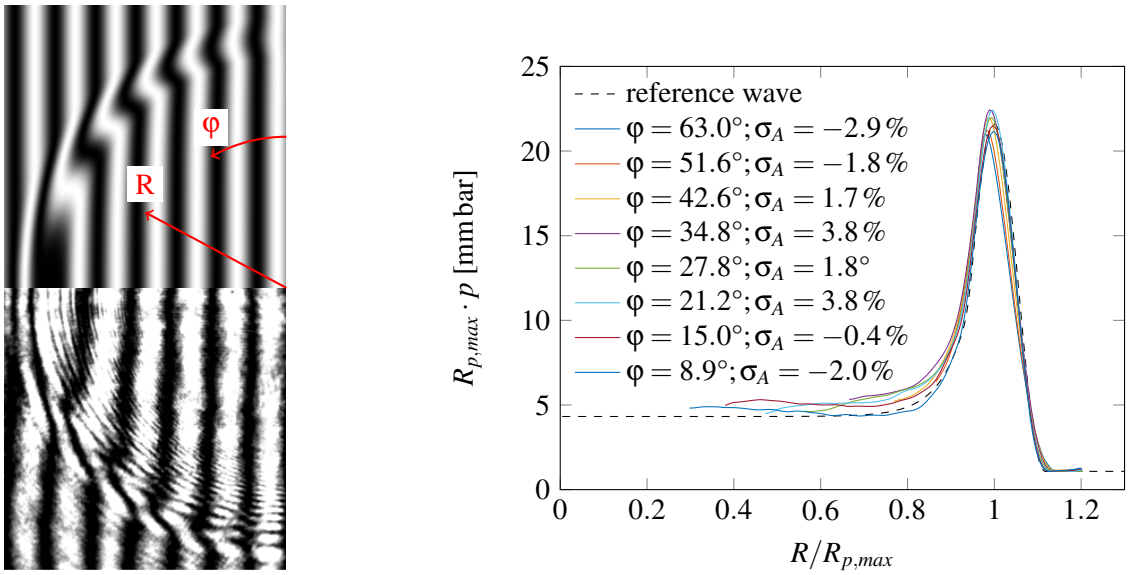

(a) (b)

Figure 2: (a) Synthetic interference pattern (top) and measured interference pattern (buttom) of a spherical pressure wave; (b) Reconstructed radial pressure distribution of the synthetic interference pattern shown at the top of (b)

radius-weighted pressure curves as function of normalized radius for different orientation angles, where $R_{p,max}$ denotes the radius at the pressure maximum and σ_A the corresponding deviation. For orientation angles $8.9° \leq \varphi \leq 63.0°$ amplitude values can be determined with an accuracy of 96.2 %. From Fig. 2(b) it is also apparent that amplitudes are slightly underestimated for small and large orientation angles while beeing overestimated for $21.2° \leq \varphi \leq 42.6°$.

4 Pressure wave and caviation bubble engergy budgets

Measurements were done in water with 96 % saturation of oxygen. 500 double images were recorded for interference measurements with a recording frequency of 0.5 Hz to minimize local heating effects of the water. The temperature increase during 17 min measurements for each data set stayed below 0.1 K. Laser energies of $22.3\,\mu J \leq E_l \leq 26.9\,\mu J$ were measured for all laser pulses with an average energy of 25.2 µJ. These created caviation bubbles with an averaged maximum bubble radius of $\bar{R}_{max} = 299\,\mu m \pm 59\,\mu m$. Interferograms had a field of view of 6.26 mm x 5.22 mm, allowing pressure waves with a time variation of approximately 3.5 µs to be recorded. Cavitation bubbles with radii between $240\,nm \leq R_{max} \leq 358\,nm$ were recorded emanating from caviation bubbles with a collapse time variation of approximately 11 µs. Thus, pressure wave events could be recorded in approximately every third interferogram. Due to a fixed starting time (the instant of bubble creation), the 1st frame always captures the pressure wave of optical breakthrough while the second one originates from bubble implosion. Pressure waves of the 1st and 2nd frames were statistically evaluated. Fig. 3(a) shows an averaged results of interference evaluations for N=66 repeated measurements. The blue line represents the pressure curve for the initial shock wave, the dashed blue lines show the corresponding standard deviation. The interferograms were selected using hydrophone measurements with pressure maxima between $16.1\,mm\,bar \leq R_{p,max} \leq 17.8\,mm\,bar$ for the first pressure wave. Results are depicted for an orientation angle $\varphi = 27.2°$. The standard deviation δ resulting from the interferometric reconstruction is 10.4 % in the pressure peak corresponding to that with the hydrophone.
Fig. 3(b) shows the results of interference measurements for hydrophone measurements between $16.5\,mm\,bar \leq R_{p,max} \cdot p \leq 16.8\,mm\,bar$ for the second pressure wave of bubble implosion. For better comparability, the pressure profiles were weighted with the radius to compensate for the pressure reduction with increasing radius. Due to the high variability, the number of comparable interferograms was limited to $N = 3$. The standard deviation of the pressure wave position was 12 % and is represented by the blue error

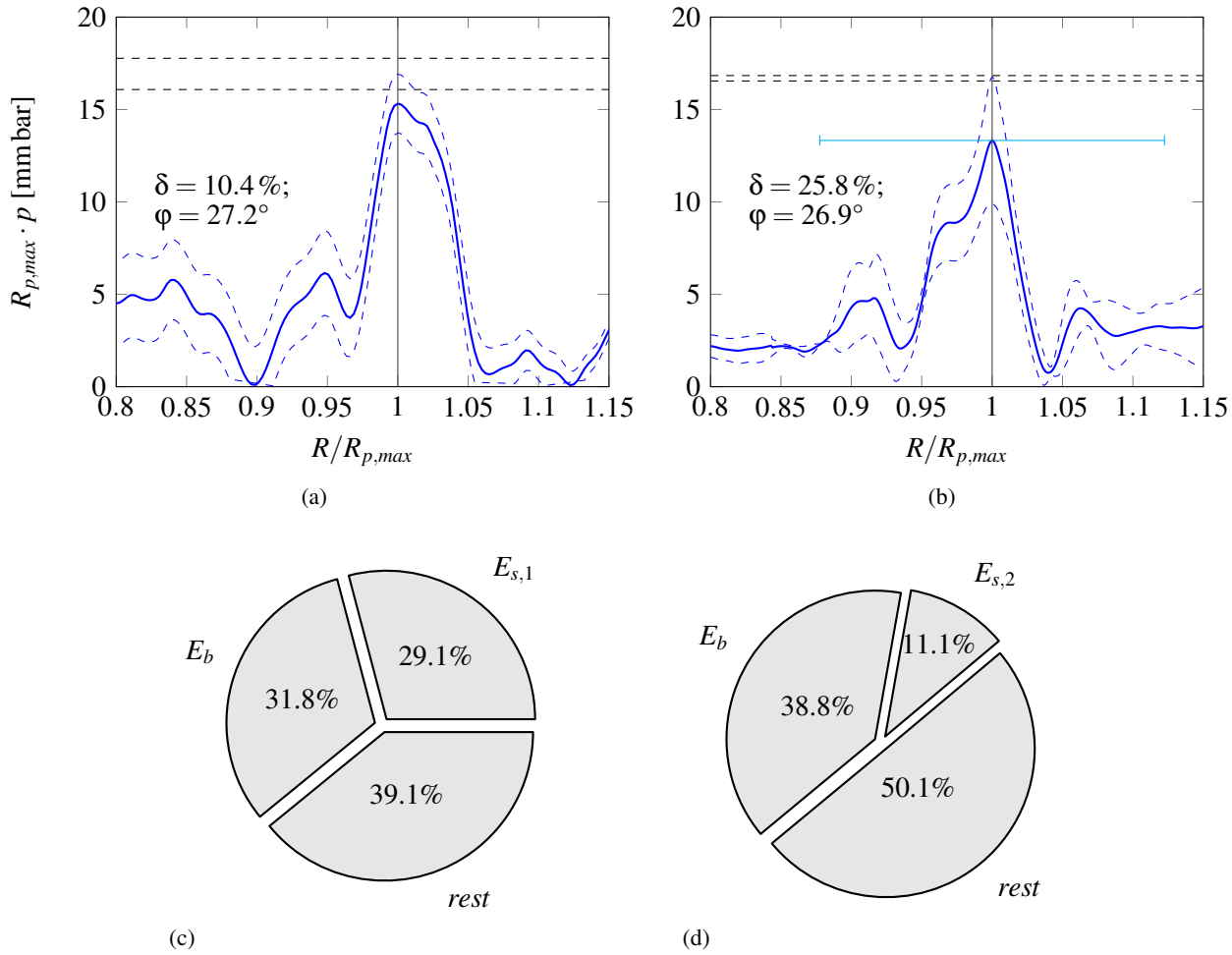

Figure 3: (a) Averaged pressure curve for N=66 of inital shock wave. Peak is at 15.3 mm bar and hydrophone measurement 16.1 mm bar $\leq R_{p,max} \cdot p \leq$ 17.8 mm bar. Errorbar shows standard deviation of R_{max};(b) Averaged pressure curve for N=3 of the shock wave after bubble collapse. Peak is at 13.3 mm bar and hydrophone measurement 16.5 mm bar $\leq R_{p,max} \cdot p \leq$ 16.8 mm bar; (c) Energy balances of initial pressure wave; (d) Energy balances of pressure waves after bubble collapse

bar. Here, the results are for an orientation angle $\varphi = 26.9°$. The standard deviation of the evaluated peak pressure is $\delta = 25.8\,\%$.
From the results of Figs. 3(a) and 3(b) energy budgets can be calculated. For the calculation of the shock wave energy E_s the pressure profiles have been integrated from the point when the pressure fell below 1 bar towards bubble center. For the pressure at $R/R_{p,max} < 0.8$ a constant mean value of the last 20 data points has been assumed. The averaged laser energy for evaluations of the inital pressure wave was measured to be $E_l = 24.5 \pm 3.2\,\mu J$. A bubble energy $E_b = 7.8\,\mu J$ and a pressure wave engergy of the optical breakthrough $E_{s,1} = 7.1\,\mu J$ at 3.85 mm distance from bubble center were calculated. In comparison, the averaged laser energy for evaluations of the pressure wave after bubble collapse for the same pressure radius was $E_l = 25.2 \pm 0.9\,\mu J$. The bubble energy was $E_b = 10.0\,\mu J$ and the pressure wave energy at a distance of 3.01 mm from bubble center was $E_{s,2} = 2.9\,\mu J$. Results are summarized in Figs. 3(c),(d).

5 Conclusion

In the present study synthetic interference images of spherical pressure wave distributions could be reconstructed with an accuracy of 96.2 % for orientation angles of $8.9° \leq \varphi \leq 63.0°$. To be able to study more complex wave dynamics, e.g. reflections of pressure waves at interfaces, an indepent measured gradient of different direction would be a great achieve. The reconstructed pressure curves from the actual measurements of initial pressure wave and pressure wave after bubble collapse were in agreement with the hydrophone measurements. Nevertheless, both cases had high standard deviations. Due to changes in the maximum bubble radius that strongly influenced the propagation length of the pressure wave. The energy balance showed that the pressure wave energy of the initial pressure wave after optical breakthrough is higher than for the pressure wave after bubble collapse.

Acknowledgements

This research was financially supported by DFG (HU 2264/1-1).

References

Kim BM, Komashko AM, Rubenchik AM, Feit MD, Reidt S, Da Silva LB, and Eichler J (2003) Interferometric analysis of ultrashort pulse laser-induced pressure waves in water. *Journal of Applied Physics* 94:709–715

Nagayama K, Mori Y, Shimada K, and Nakahara M (2002) Shock Hugoniot compression curve for water up to 1 GPa by using a compressed gas gun. *Journal of Applied Physics* 91:476

Shen YR (1984) *The principles of nonlinear optics*. J. Wiley, New York

Veysset D, aznev AA, Pezeril T, Kooi S, and Nelson KA (2016) Interferometric analysis of laser-driven cylindrically focusing shock waves in a thin liquid layer. *Scientific Reports* 6

Vogel A (1996) Shock wave emission and cavitation bubble generation by picosecond and nanosecond optical breakdown in water. *The Journal of the Acoustical Society of America* 100:148

Vogel A and Lauterborn W (1988) Acoustic transient generation by laser-produced cavitation bubbles near solid boundaries. *The Journal of the Acoustical Society of America* 84:719–731

Ward B and Emmony D (1991) Interferometric studies of the pressures developed in a liquid during infrared-laser-induced cavitation-bubble oscillation. *Infrared Physics* 32:489–515